Modeling Quiescent Phase Transport of Air Bubbles Induced by Breaking Waves

BY

FENGYAN SHI, JAMES T. KIRBY AND GANGFENG MA

RESEARCH REPORT NO. CACR-10-05
JUNE 2010

CENTER FOR APPLIED COASTAL RESEARCH

Ocean Engineering Laboratory
University of Delaware
Newark, Delaware 19716

Modeling Quiescent Phase Transport of Air Bubbles Induced by Breaking Waves

Fengyan Shi, James T. Kirby and Gangfeng Ma
Center for Applied Coastal Research, University of Delaware, USA.

Abstract

Simultaneous modeling of both the acoustic phase and quiescent phase of breaking wave-induced air bubbles involves a large range of length scales from microns to meters and time scales from milliseconds to seconds, and thus is computational unaffordable in a surfzone-scale computational domain. In this study, we use an air bubble entrainment formula in a two-fluid model to predict air bubble evolution in the quiescent phase in a breaking wave event. The breaking wave-induced air bubble entrainment is formulated by connecting the shear production at the air-water interface and the bubble number intensity with a certain bubble size spectra observed in laboratory experiments. A two-fluid model is developed based on the partial differential equations of the gas-liquid mixture phase and the continuum bubble phase, which has multiple size bubble groups representing a polydisperse bubble population. An enhanced 2-DV VOF (Volume of Fluid) model with a $k-\epsilon$ turbulence closure is used to model the mixture phase. The bubble phase is governed by the advection-diffusion equations of the gas molar concentration and bubble intensity for groups of bubbles with different sizes. The model is used to simulate air bubble plumes measured in laboratory experiments. Numerical results indicate that, with an appropriate parameter in the air entrainment formula, the model is able to predict the main features of bubbly flows as evidenced by reasonable agreement with measured void fraction. Bubbles larger than an intermediate radius of $O(1\text{mm})$ make a major contribution to void fraction in the near-crest region. Smaller bubbles tend to penetrate deeper and stay longer in the water column, resulting in significant contribution to the cross-sectional area of the bubble cloud. An under-prediction of void fraction is found at the beginning of wave breaking when large air-pockets take place. The core region of high void fraction predicted by the model is dislocated due to use of the shear production in the algorithm for initial bubble entrainment. The study demonstrates a potential use of an entrainment formula in simulations of air bubble population in a surfzone-scale domain. It also reveals some difficulties in use of the two-fluid model for predicting large air pockets induced by wave breaking, and suggests that it may be necessary to use a gas-liquid two-phase model as the basic model framework for the mixture phase and to develop an algorithm to allow for transfer of discrete air pockets to the continuum bubble phase. A more theoretically justifiable air entrainment formulation should be developed.

Keywords: air bubble, breaking wave, RANS model

1. Introduction

The simulation of breaking wave-induced bubbly flows is a great challenge due to the complexity of air entrainment and bubble evolution processes, and to the range of spatial and temporal scales involved. According to previous studies based on field or laboratory experiments (e.g., Thorpe, 1982; Garrett et al., 2000; Terrill et al., 2001; Deane and Stokes, 2002), the lifetime of wave-generated bubbles can be categorized into two phases. The first phase is called the acoustic phase, during which bubbles are entrained and fragmented inside the breaking wave crest. The second phase happens after bubble creation processes cease and the newly formed bubbles evolve under the influence of turbulent diffusion, advection, buoyant degassing, and dissolution. Because this phase is acoustically quiescent, it is called the quiescent phase. The duration of the acoustic phase is very short and the time scale of bubble fragmentation is typically tens of milliseconds (Leighton, et al., 1994). Therefore, Direct Numerical Simulations (DNS) of the acoustic phase require higher resolution in both time and space in order to capture the details of the air entrainment process, making computations so expensive that the main use of this kind of model will be limited to applications to studies of bubble creation mechanisms.

Instead of a direct simulation of the air entrainment process, the use of an initial air entrainment formulation in modeling of bubbly flows was reported recently (Moraga et al., 2008; Shi et al., 2008). The idea was to prescribe air bubbles entrained during the acoustic phase in a two-phase model using a bubble entrainment formulation. The model fed with the initially entrained bubbles simulates bubble plumes and requires much less spatial and temporal resolution than needed to capture the air entrainment process. The initial bubble number density and bubble size distribution were formulated based on theoretical and observational studies.

In a simulation of air bubbles entrained by naval surface ships, Moraga et al. (2008) presented a sub-grid model that detects the location of the air bubble entrainment region. The localized region of high void fraction is bounded by the surface at which the downward liquid velocity reaches a certain value (0.22 m/s was used in Moraga et al.'s application). The initial bubble size distribution in the localized region follows the bubble size spectrum measured by Deane and Stokes (2002) who suggested that, at the beginning of the quiescent phase, the size spectrum follows a certain power-law scaling with bubble radius. Deane and Stokes (2002) found two distinct mechanisms controlling the size distribution, depending on bubble size. For bubbles larger than the Hinze scale (about 1 mm in Deane and Stokes (2002)), turbulent fragmentation determines bubble size distribution, resulting in a bubble density proportional to $r_b^{-10/3}$, where r_b is bubble radius. Bubbles smaller than the Hinze scale are generated by jet and drop impact on wave face, with a bubble density proportional to $r_b^{-3/2}$. The Hinze scale, which separates the two processes, is the scale where turbulent fragmentation ceases, and is related to the turbulent dissipation rate and the surface tension. A parallel study was carried out by Shi et al. (2008), who used the same strategy to avoid modeling of the bubble entrainment process, but applied a different air entrainment formulation for breaking wave-induced air bubbles. The initial air bubble entrainment is formulated by connecting the flow shear stress at air-water interface and the bubble number intensity with the bubble size spectra as observed by Deane and Stokes (2002). The model was used to simulate wave transformation, breaking, and bubble generation and evolution processes over a barred beach in the Large Wave Flume at Oregon State University. Although there were no data for bubble quantities for comparison, the model results showed that the evolution pattern of void fraction at the water surface is consistent with bubble foam signatures sensed by video systems during the laboratory experiments. The study showed the potential to use an air entrainment formulation in modeling of air bubbles inside the surfzone.

Models based on the volume or ensemble averaged two-fluid approach seem best suited for practical use in modeling air bubbles in large-scale systems such as breaking wave-induced bubbles in coastal water because of their efficiency (Sokolichin et al., 2004). Carrica et al. (1998) reported a multiphase model for simulating bubbly two-phase flow around a surface ship. The bubble phase is modeled using the integrated Boltzmann transport equation for the bubble size distribution function (Guido-Lavalle et al., 1994) and the momentum equations for the gaseous phase. The liquid phase is modeled using mass and momentum equations for liquid along with a turbulence closure. The gas-liquid interactions are represented by drag, pressure, lift and buoyancy forces. The model accounts for intergroup bubble transfer through bubble coalescence, dissolution and breakup. The recent work of Moraga et al. (2008) followed the approach of Carrica et al. (1998). A similar approach is used by Buscaglia et al. (2002) who developed a double-averaged multiphase model without taking into account the momentum balance in the bubble phase. The exclusion of momentum equations for the bubble phase makes the model more efficient, especially in a simulation involving a number of bubble groups with different sizes. Shi et al. (2008) used the method of Buscaglia et al. (2002) in the preliminary investigation of air bubbles generated by breaking waves inside the surfzone. Although Carrica et al.'s approach is more rigorous in theory in terms of the Favre-averaging, Buscaglia et al.'s method still remains a valuable alternative as a computational efficient model for practical purposes.

The focus of the present study is to estimate bubble population evolution and spatial distribution in a breaking wave event. Due to the complexity of wave breaking processes and the lack of sufficient knowledge of bubble entrainment and water-bubble interaction, we intend to develop a simple and physically based model. We will show developments of the model based on Buscaglia et al. (2002) and components representing bubble coalescence, breakup and bubble-induced turbulence effects. The model is tested against laboratory data reported by Lamarre and Melville (1991), referred to hereafter as LM91.

2. TWO FLUID MODEL

Buscaglia et al. (2002) derived a two-fluid model using a double-averaging approach. The first average was performed at spatial scales of the order of the bubble-to-bubble spacing L_{bb} and resulted in mass and momentum conservation equations for a gas-liquid mixture. The second average was carried out using Reynolds averaging over the gas-liquid mixture equations at larger turbulence scales. The governing equation for the bubble phase was the Reynolds-averaged mass balance equation, taking into account bubble diffusion due to turbulence. The two-fluid model of Buscaglia et al. (2002) involves a liquid chemistry process which incorporates oxygen and nitrogen dissolution in applications to bubble plumes. Two bubble groups, i.e., oxygen group and nitrogen group, with a uniform bubble size were considered. No bubble breakup or coalescence is taken into account in their model.

In this section, we review the basic equations of the two-fluid model derived by Buscaglia et al. (2002). Some modifications and additions are made in order to represent polydisperse bubble population, bubble-induced turbulence, bubble breakup and coalescence.

2.1. Mixed Fluid Phase

The double-averaged equations include mass conservation and momentum equations for the mixture fluid phase:

$$\nabla \cdot \mathbf{u}_m = 0 \tag{1}$$

$$\frac{\partial \mathbf{u}_m}{\partial t} + \mathbf{u}_m \cdot \nabla \mathbf{u}_m + \frac{1}{\rho_0}\nabla P_m = \frac{1}{\rho_0}\nabla \cdot (2\mu_t \mathbf{S}) - \frac{\rho_m}{\rho_0} g\mathbf{k} \tag{2}$$

where $\mathbf{u}_m, P_m$ and ρ_m represent the mixture quantities of fluid velocity, pressure and density, respectively. $\mathbf{k}$ is a vertical unit vector. ρ_0 is a reference density which has replaced ρ_m in all terms but the gravity term using the Boussinesq approximation. It is noted that the Boussinesq approximation is invalid for the mixture fluid with a high and inhomogeneous distribution of void fraction. It is assumed in the present study that high void fraction is localized within a limited region so that the pressure gradient caused the spatial variation in density would not affect much the overall wave form evolution. The assumption is confirmed to be appropriate in the numerical results shown in section 3.2.

$\mathbf{S}$ represents the rate of strain tensor of the mean flow defined by

$$\mathbf{S} = \frac{1}{2}(\nabla \mathbf{u}_m + \nabla^T \mathbf{u}_m), \tag{3}$$

μ_t is the eddy viscosity coefficient which is related to turbulent kinetic energy, k, and turbulent dissipation, ϵ, in the $k - \epsilon$ turbulence equations shown in Section 2.3. The relation between k and ϵ can be expressed by

$$\mu_t = \rho_0 C_\mu \frac{k^2}{\epsilon} \tag{4}$$

where C_μ is an empirical coefficient and $C_\mu = 0.09$ was used as suggested by Rodi (1980).

The last term in (2) represents the buoyancy force which can be evaluated by

$$\frac{\rho_m}{\rho_0} g\mathbf{k} = (1 - \alpha_b) g\mathbf{k} \tag{5}$$

where α_b is the volume fraction of bubbles following the definition in Drew and Passman (1998).

2.2. Bubble Phase

In this study, we do not employ the multicomponent gas model and associated chemistry framework of Buscaglia et al. (2002). Instead, we consider the gas to be a single, inert component, and we neglect dissolution of the gas phase in water. The bubble population is split into NG groups based on bubble radius. The equations for the bubble phase include the equations of the gas molar concentration and bubble number density with different bubble sizes. Bin i of the bubble population is calculated using simple advection-diffusion equations given by

$$\frac{\partial C_{b,i}}{\partial t} + \nabla \cdot (C_{b,i} \mathbf{u}_g) = \mathcal{E}_{c,i} + \mathcal{S}_{c,i} + \nabla \cdot (\mathcal{D}_g \nabla C_{b,i}) \tag{6}$$

$$\frac{\partial N_{b,i}}{\partial t} + \nabla \cdot (N_{b,i} \mathbf{u}_g) = \mathcal{E}_{n,i} + \mathcal{S}_{n,i} + \nabla \cdot (\mathcal{D}_g \nabla N_{b,i}) \tag{7}$$

where $C_{b,i}$ and $N_{b,i}$ represent, respectively, the gas molar concentration and bubble number per unit volume for bubble size i. The total gas molar concentration and bubble number per unit volume are, respectively,

$$C_b = \sum_{i=1}^{NG} C_{b,i}, \tag{8}$$

and

$$N_b = \sum_{i=1}^{NG} N_{b,i}. \tag{9}$$

$\mathbf{u}_g$ is the bubble advection velocity which can be calculated by

$$\mathbf{u}_g = \mathbf{u}_m + w_s(r_b)\mathbf{k} \tag{10}$$

in which $w_s(r_b)$ is the bubble-slip velocity, assumed to depend on the bubble radius following Clift et al. (1978):

$$w_s = \begin{cases} 4474 \text{ m/s} \times r_b^{1.357} & \text{if } 0 \leq r_b \leq 7 \times 10^{-4} m \\ 0.23 \text{ m/s} & \text{if } 7 \times 10^{-4} < r_b \leq 5.1 \times 10^{-3} m \\ 4.202 \text{ m/s} \times r_b^{0.547} & \text{if } r_b > 5.1 \times 10^{-3} m \end{cases} \tag{11}$$

$\mathcal{E}_{c,i}$ and $\mathcal{E}_{n,i}$ are source terms associated with bubble entrainment. $\mathcal{S}_{c,i}$ and $\mathcal{S}_{n,i}$ are source/sink terms associated with inter-group adjustment of bubble quantity between different component i caused by bubble size changes due to pressure change, bubble breakup and coalescence, and will be described in the following sections. $\mathcal{D}_g$ is the dispersion coefficient associated with the turbulence and bubble-bubble interaction. In the isotropic model proposed by Carrica et al. (1998),

$$\mathcal{D}_g = \frac{\mu_t}{\rho_0 S_g} \tag{12}$$

where S_g is the Schmidt number for gas (Buscaglia et al., 2002). The gas volume fractions used in (5) can be calculated using

$$\alpha_b = \frac{\mathcal{R} T_g \sum_i C_{b,i}}{P_g} \tag{13}$$

where $\mathcal{R}$ is the universal gas constant, 8.314 J/mol K. T_g is the absolute gas temperature, P_g is gas pressure, assumed equivalent to P_m. The bubble radius can be calculated using

$$r_{b,i} = \left(\frac{3\nu_{b,i}}{4\pi} \right)^{1/3} \tag{14}$$

where $\nu_b(i)$ is the bubble volume of component i which can be obtained by

$$\nu_{b,i} = \frac{C_{b,i} \mathcal{R} T_g}{P_g N_{b,i}} \tag{15}$$

In Shi et al. (2008), both the gas molar concentration equation (6) and bubble number intensity equation (7) for each group were solved in order to take into account the intergroup transfer caused by ambient pressure change. In applications of surface wave breaking in shallow water, both spatial and temporal variations in pressure field are small with respect to the atmospheric pressure at the water surface. For example, in the following application of a laboratory experiment, $\Delta P_m/P_0 < 0.07$, where P_0 is atmospheric pressure, resulting in at most 2% radius variation due to pressure changes. It was found no intergroup transfer caused by pressure changes in the laboratory case. Although both of (6) and (7) are implemented in the model for general applications, only (7) was solved for the bubble phase in the present application for a purpose of efficiency. The void fraction is calculated by

$$\alpha_b = \sum_i N_{b,i}\nu_{b,i} \tag{16}$$

where $\nu_{b,i}$ may be obtained using the relation between $\nu_{b,i}$ and $r_{b,i}$, i.e., equation (14), under the assumption that bubble size is independent of gas pressure and temperature.

2.3. Turbulence Model

Previous studies on turbulence modeling for two-phase flows indicated significant challenges in developing a suitable coupled regime between turbulent eddies and air bubbles with less knowledge in physical mechanism and scarce experimental studies (Banerjee, 1990). Turbulence plays an important role in the non-linear process of bubble breakup and coalescence, whose feedback, in turn, will affect the turbulent kinetic energy production (Sheng and Irons, 1993, Smith, 1998). In applications using transport equations for turbulence quantities, such as the $k-\epsilon$ model, a simple extension for the water-bubble two phase flows is to modify the $k-\epsilon$ model by adding some source terms in the balance equations for k and ϵ. This is based on the assumption that the shear-induced and bubble-induced turbulence effects are decoupled, so that the bubble-induced turbulence can be evaluated separately based on semi-empirical formulations (Kataoka and Serizawa, 1989, Lopez de Bertodano et al., 1994). The $k-\epsilon$ equations may be written as

$$\frac{\partial k}{\partial t}+\nabla\cdot(k\mathbf{u}_m)=\nabla\cdot\left[(\mu_0+\frac{\mu_t}{\sigma_k})\nabla k\right]+\mu_t|\mathbf{S}|^2-\epsilon+S_k \tag{17}$$

and

$$\frac{\partial \epsilon}{\partial t}+\nabla\cdot(\epsilon\mathbf{u}_m)=\nabla\cdot\left[(\mu_0+\frac{\mu_t}{\sigma_\epsilon})\nabla \epsilon\right]+C_{1\epsilon}\mu_t|\mathbf{S}|^2\frac{\epsilon}{k}-C_{2\epsilon}\frac{\epsilon^2}{k}+S_\epsilon \tag{18}$$

where μ_0 is the molecular kinematic viscosity; $\sigma_k, \sigma_\epsilon, C_{1\epsilon}$ and $C_{2\epsilon}$ are empirical coefficients with recommended values (Rodi, 1980)

$$\sigma_k=1.0, \quad \sigma_\epsilon=1.3, \quad C_{1\epsilon}=1.44, \quad C_{2\epsilon}=1.3 \tag{19}$$

S_k and S_ϵ represent source/sink terms associated with bubble-induced turbulence effects. In this study, Kataoka and Serizawa's (1989) approach is employed, which uses

$$S_k=-C_k\alpha_g\nabla p\cdot\mathbf{w}_s \tag{20}$$

$$S_\epsilon=C_\epsilon\cdot\frac{\epsilon}{k}S_k \tag{21}$$

where $\mathbf{w}_s=w_s\mathbf{k}$ and the slip velocity for a bubble radius of $1mm$ was adopted in this study, and values of coefficients C_k and C_ϵ are taken as 1.0.

2.4. Bubble Entrainment

Studies of bubble characteristics under breaking waves have indicated that the initial bubble entrainment and distribution are related to turbulence in the entraining fluid (Thorpe, 1982; Baldy, 1993; Garrett et al., 2000; Mori et al., 2007). Baldy (1993) suggested that the bubble formation rate depends on turbulent dissipation ϵ and the bubble formation energy. He gave a dimensional parameter-based source function which is linearly proportional to ϵ. Garrett et al. (2000) pointed out that, based on dimensional analysis, the bubble size spectrum should behave according to $\epsilon^{-1/3} r^{-10/2}$ for a given air volume entrained by breaking waves. Laboratory experiments by Cox and Shin (2003) showed the dependence of void fraction on turbulence intensity in the bore region of surf zone waves. Mori et al. (2007) show a linear relationship between the void fraction and turbulence intensity in their experimental study. Although the construction and parameterization of a quantitative source function may be uncertain because of the lack of detailed observation, there is a general belief that bubble formation and initial size distribution are related to turbulence. It is our understanding that, in a wave breaking event, bubble generation is dependent on the intensity of wave breaking and types of breakers. For plunging breakers, the major entrained air volume is from an air pocket formed by a plunging jet impinging ahead of the wave face. The injected air packet is broken up by turbulence into small bubbles. For spilling breakers, air bubbles are entrained by a surface roller and penetrate into the water column. At the beginning of the quiescent phase, a statistical equilibrium in bubble size distribution is achieved with an initial size spectrum of a power law (Garrett et al., 2000, Deane and Stokes, 2002).

The complexity of the bubble entrainment process and lack of knowledge of the bubble entrainment mechanism make the formulation of a bubble entrainment source function difficult. It is natural to start with a simple source function to model bubbles entrained by breaking waves. In this study, we model the initial bubble entrainment by connecting the production of turbulent kinetic energy at the air-water interface and the bubble number intensity with certain bubble size spectra observed by Deane and Stokes (2002). The increment of initial bubble number per unit radius increment can be written as

$$dN_{b,i} = a_b P_r D_i dt, \qquad P_r > P_{r0} \tag{22}$$

where a_b is a constant to be determined, P_r is the shear production term, i.e., $P_r = \mu_t |\mathbf{S}|^2$, P_{r0} is a threshold for the onset air entrainment, D_i is the bubble size probability function. Based on Deane and Stokes (2002), the bubble density per unit radius increment can by calculated by

$$N = \begin{cases} N_H \left(\frac{r_b}{r_H}\right)^{-3/2}, & r_{b,min} \leq r_b \leq r_H \\ N_H \left(\frac{r_b}{r_H}\right)^{-10/3}, & r_H < r_b \leq r_{b,max} \end{cases} \tag{23}$$

where $r_{b,min}$ and $r_{b,max}$ represent respectively the minimum and maximum bubble radius considered, N_H is the bubble density per unit radius increment at the Hinze scale r_H (Hinze, 1955). Based on the formula of Hinze (1955), the Hinze scale is a function of the turbulent dissipation, surface tension and the critical Weber number. The relationship between bubble size distribution and the intermittent dissipation rate or the average dissipation rate were discussed in Garrett et al. (2000). In this study, we adopted $r_H = 1\ mm$, which was measured in Deane and Stokes (2002) rather than computed from the model. r_H values estimated from computed dissipation rates in the model fall in the range of $1 - 1.5mm$ in the region of established breaking described below, and are thus consistent with the value $r_H = 1mm$ which we apply uniformly. The probability function D_i may be obtained using the bubble density N normalized by the maximum N which is the value at $r_{b,min}$:

$$D_i = \begin{cases} r_{b,min}^{3/2} r_{b,i}^{-3/2}, & r_{b,min} \leq r_{b,i} \leq r_H \\ r_{b,min}^{3/2} r_H^{11/6} r_{b,i}^{-10/3}, & r_H < r_b \leq r_{b,max} \end{cases} \tag{24}$$

Figure 2 demonstrates an example of D_i with 20 bins of bubbles, $r_{b,min} = 0.1\ mm$ and $r_{b,max} = 10\ mm$. This example will be used in the following application in Section 3.

According to (22), the source term $\mathcal{E}_n$ can be written as

$$\mathcal{E}_{n,i} = a_b P_r D_i dr_{b,i} \qquad P_r > P_{r0} \tag{25}$$

where $dr_{b,i}$ is the radius spacing of bin i. For given $r_{b,i}$, $\mathcal{E}_{n,i}$ and P_g, the source term in the molar concentration equation $\mathcal{E}_{c,i}$ is calculated using the ideal gas law (14) and and the relation between $r_{b,i}$ and $\nu_{b,i}$ (15). In our applications, the molar concentration was not calculated as described in Section 2.2.

2.5. Bubble Coalescence and Breakup

Since only (7) was applied as the governing equation for the bubble phase in our application, only the source term $\mathcal{S}_{n,i}$ was taken into account for the intergroup transfer due to the bubble coalescence and breakup. It can be written as

$$\mathcal{S}_{n,i} = \chi_i^+ - \chi_i^- + \beta_i^+ - \beta_i^- \tag{26}$$

where $\chi_i^\pm$ and $\beta_i^\pm$ represent source/sink due to the coalescence and breakup, respectively. According to Prince and Blanch (1990), the coalescence source which represents the gain in bubble group i due to coalescence of smaller bubbles is given by

$$\chi_i^+ = \frac{1}{2}\sum_{k,l<i} T_{kl}\zeta_{kl}X_{ikl} \tag{27}$$

where T_{kl} is the collision rate of bubble group k and l which can be evaluated by

$$T_{kl} = \frac{\sqrt{2}}{4}\pi(2r_{b,k} + 2r_{b,l})^2\epsilon^{1/3}\left[(2r_{b,k})^{2/3} + (2r_{b,l})^{2/3}\right]^{1/2} N_{b,k}N_{b,l} \tag{28}$$

ζ_{kl} is the coalescence efficiency which represents the probability of coalescence when collision occurs. Based on Lou (1993), ζ_{kl} is given by

$$\zeta_{kl} = \exp\left\{ -\frac{\left[0.75(1+(r_{b,k}^2/r_{b,l}^2)(1+r_{b,k}^3/r_{b,l}^3)\right]^{1/2}}{(\rho_g/\rho_0+0.5)^{1/2}(1+r_{b,k}/r_{b,l})^3} W_{kl}^{1/2} \right\} \tag{29}$$

where ρ_g is air density; W_{kl} is the Weber number (see Luo, 1993 or Chen et al., 2005). The last item in (27), X_{ikl}, is the number of bubble transfered from the coalescence of two bubbles from group k and l to group i

$$X_{ikl} = \frac{\nu_k+\nu_l-\nu_{i-1}}{\nu_i-\nu_{i-1}} \qquad \nu_{i-1} < \nu_k+\nu_l < \nu_i \tag{30}$$

$$X_{ikl} = \frac{\nu_{i+1}-(\nu_k-\nu_l)}{\nu_{i+1}-\nu_i} \qquad \nu_i < \nu_k+\nu_l < \nu_{i+1} \tag{31}$$

The sink caused by coalescence in group i can be calculated by

$$\chi_i^- = \sum_{k=1}^{NG} T_{ik}\zeta_{ik} \tag{32}$$

The source term of bubble breakup is calculated by

$$\beta_i^+ = \sum_{k=i}^{NG} \phi_k X_{ik} \tag{33}$$

where ϕ_k is a breakup kernal function given by Luo and Svendsen (1996),

$$\phi_k = c_b\alpha_b N_{b,k}\left(\frac{\epsilon}{4r_{b,k}^2}\right)^{1/3} \int_{\xi_{min}}^{1} \frac{(1+\xi)^2}{\xi^{11/3}} \times \exp\left[-\frac{12c_f\sigma}{\gamma\rho_0\epsilon^{2/3}(2r_b)^{5/3}\xi^{11/3}}\right] d\xi \tag{34}$$

in which c_b, γ and c_f are constants and $c_b = 0.923$, $c_f = 0.2599$, and $\gamma = 2.04$ in this study, σ is surface tension, ξ is the dimensionless eddy size and ξ_{min} is the minimum value of γ which can be obtained using the minimum eddy size given by van den Hengel et al. (2005):

$$\lambda_{min} = 11.4 \left(\frac{\mu_0^3}{\epsilon} \right)^{1/4} \tag{35}$$

We assume that the breakup splits a bubble into two identical daughter bubbles thus that X_{ik} can be written as

$$X_{ik} = 2\frac{\nu_k/2 - \nu_{i-1}}{\nu_i - \nu_{i-1}} \qquad \nu_{i-1} < \nu_k/2 < \nu_i \tag{36}$$

$$X_{ik} = 2\frac{\nu_{i+1} - \nu_k/2}{\nu_{i+1} - \nu_i} \qquad \nu_{i+1} > \nu_k/2 > \nu_i \tag{37}$$

$$X_{ik} = 0 \qquad \text{otherwise} \tag{38}$$

The sink term of bubble breakup is calculated using

$$\beta_i^- = \phi_i \tag{39}$$

It should be mentioned that there are other bubble breakup and coalescence models to choose for this study. For example, our newly developed 3D model (Ma et al., 2010, in preparation) with the similar air entrainment approach utilizes the model of Martínez-Bazán (1999). Because of the purpose of this paper, the differences in using different models and effects of bubble breakup and coalescence are not discussed. Interested readers can refer to Lasheras et al. (2002) and Chen et al. (2005).

2.6. Model implementation

We use the 2-D VOF model RIPPLE (Kothe et al., 1991) as the basic framework for the computational code. The VOF model is a single phase model and has been enhanced with several different turbulence closure models such as $k-\epsilon$ model (Lin and Liu, 1998) and multi-scale LES (Large Eddy Simulation) model (Zhao et al., 2004, Shi et al., 2004). In this study, we adopted the $k-\epsilon$ approach with extra source terms, S_k and S_ϵ, to account for bubble-induced turbulence effects. The buoyancy force was added in the model using formula (5) in which the void fraction α_b may be evaluated using (16). The governing equation for the bubble number intensity (7) of each bubble group was implemented using the standard numerical scheme for advection-diffusion equation which exists in the VOF code.

3. APPLICATION TO BREAKING WAVE EXPERIMENT OF LAMARRE AND MELVILLE (1991)

We test the capabilities of the present model by comparing to experimental data on an isolated breaking event, as studied in laboratory conditions by Rapp and Melville (1990) and LM91. The wave breaking event in this study is generated in a narrow flume and is mainly two-dimensional, aside from complex flow structures generated in the breaking wave crest, and is thus reasonably well suited for study by the present two-dimensional model.

3.1. Model setup and test runs

LM91 conducted measurements of air bubbles entrained by controlled breaking waves in a wave flume 25 m long and 0.7 m wide filled with fresh water to a depth of 0.6 m. Breaking waves were produced by a piston-type wave maker generating a packet of waves with progressively decreasing frequency (Rapp and Melville, 1990), leading to a focussing of wave energy at a distance $x_f = 8.46\ m$ from the wave paddle. The wave packet was composed of $N = 32$ sinusoidal components of slope $a_i k_i$ where a_i and k_i are the amplitude and wave number of the ith component. Based on the linear composition, the surface displacement is

$$\eta(x,t) = \sum_{i=1}^{N} a_i \cos[k_i(x - x_f) - 2\pi f_i(t - t_f)] \tag{40}$$

where f_i is the frequency of the ith component; x_f and t_f are the location and time of focusing, respectively. In the experiments, the discrete frequencies f_i were uniformly spaced over the band $\Delta f = f_N - f_1$ with a central frequency defined by $f_c = \frac{1}{2}(f_N - f_1)$. The wave packet envelope steepness may be evaluated by $\Delta f / f_c$. In the numerical study, we use a computational domain with dimensions of 30 m in the horizontal direction and 0.8 m in the vertical direction. The coordinates are specified in $x = -10 \sim 20m$ and $z = -0.6 \sim 0.20m$ with the still water level at $z = 0$ and with $x = 0$ corresponding to the wavemaker position. An internal wave maker (Lin and Liu, 1999) was applied at $x = 0$ and generates the wave packet based on (40). A sponge layer with a width of 5 m was used at each end of the domain to avoid wave reflection from the boundaries. The computational domain is discretized into 1501 × 201 nonuniform cells with a minimum spacing of 0.01 m in 4 m $\leq x \leq$ 10 m, and 201 cells in z direction with a minimum spacing of 0.0025 m at $z > 0$ m, as shown in Figure 1.

Based on sensitivity tests on bubble group numbers, we adopted 20 groups of bubbles with the smallest radius $r_{b,min} = 10^{-1}$ mm and the largest radius $r_{b,max} = 10$ mm. The other 18 bubble radii were obtained by equal splitting in the logarithm of bubble radius between 10^{-1} and 10 mm and are respectively 0.13, 0.16, 0.21, 0.26, 0.34, 0.43, 0.55, 0.70, 0.89, 1.13, 1.43, 1.83, 2.33, 2.98, 3.79, 4.83, 6.16, and 7.85 mm. The bubble size probability density function with respect to the 20 bubble sizes can be obtained based on (24) and is shown in Figure 2.

In the laboratory experiments, $f_c = 0.88$ and $\Delta f/f_c = 0.73$ were used and constant amplitude, i.e.,$a_i = a_c$, was specified. In the numerical study, we carried out two cases, one with $a_c k_c = 0.38$, corresponding to the case where void fraction was measured and used for analysis in LM91, the other with $a_c k_c = 0.352$, corresponding to the case for which photographs of the bubble cloud are given by Rapp and Melville (1990). Here, k_c is the central wave number corresponding to f_c.

In order to calibrate the model, we performed a series of model test runs with different adjustable parameters, a_b, P_{r0}, and S_g, towards the model results best suited to the measured data. In LM91, void fractions of $> 20\%$

for several test cases were observed for up to half a wave period after breaking. The void fractions near the surface can reach $40 \sim 50\%$ (measured at $0.26T$,where T is the wave period, shown in Figure 3a in LM91). Among the adjustable parameters, a_b was found to be the most sensitive parameter for the overall void fraction level due to its representation of the air entrainment rate. Therefore, we focussed on the adjustment of a_b and adopted fixed parameters $P_{r0} = 0.02\ m^2/s^3$ and $S_g = 0.7$ in all test runs. Figure 3 shows the maximum void fractions with respect to different a_b chosen for test cases. A nearly linear relation between a_b and the maximum void fraction was observed. The parameter $a_b = 1.45 \times 10^9$ predicted the maximum void fraction of 40% which generally suits for the maximum void fraction level observed in the laboratory experiments. It was used to generate numerical results for comparisons with the measured data.

3.2. Model results

Figure 4 shows predicted wave breaking patterns and contours of the void fraction above 0.1%, with comparisons to photo images (first and third column) of the bubble cloud taken in the laboratory experiments in the case of $ak_c = 0.352$. The model predicts a wave break point which is about one wave length upstream of the focal point $x_f = 8.46\ m$, as observed in the laboratory experiments. The predicted water surface evolution agrees well with that shown in the images. Patterns of predicted void fraction contours generally match the images of the bubble cloud, although the predicted void fraction distribution does not contain some of the structural detail apparent in the photographed bubble cloud. Some bubble cloud deepening patterns shown in the images in $t = 19.30 \sim 19.50\ s$ were not observed in the modeled distribution of void fraction. These patterns may be caused by three dimensional effects including obliquely descending eddies (Nadaoka et al., 1989).

Predicted air entrainment is directly connected to shear production in the entrainment formula (25). Results for bubble number density (above 5×10^6) and the corresponding shear production above the threshold $P_{r0} = 0.02\ m^2/s^3$ are shown in Figure 5. The water surface elevation and elapsed time shown in the figure were normalized respectively by central wave number k_c and wave period T associated with the central frequency f_c. t_b is the time at breaking, which was approximately determined by the time when the turbulent production started to increase significantly. When the wave starts to break, bubbles are entrained at the wave crest and bubble number density is localized in a small area. As the breaking bore moves forward, the wave height drops rapidly, accompanied by more intense shear production leading to more significant bubble entrainment. The shear production above the air entrainment threshold is persistently located at the breaking wave crest with a moderate time variation in its value, while the bubble number density varies by an order of magnitude over an elapsed time corresponding to a wave period. The distribution of bubble number intensity indicates that bubbles spread downstream and form a long tail of the bubble cloud beneath the wave surface.

Following LM91, who used 0.3% void fraction as a threshold to evaluate the volume of entrained air, we show snapshots of distribution of void fraction above the threshold 0.3% in Figure 6. The figure shows that, at beginning of wave breaking, air is entrained at the wave crest and the area bounded by the threshold 0.3% is small. The bounded area increases as the wave moving forward and reaches a maximum around the half wave period. After the maximum area is reached, the overall void fraction decreases due to the degassing process. The higher void fraction can be found at the leading bore followed by a long tail of lower void fraction.

In LM91, several moments of the void fraction field were computed from void fraction measurements according to the following definitions,

$$A = \int_A dA, \tag{41}$$

$$V = \int_A \alpha_b dA, \tag{42}$$

and

$$\bar{\alpha}_b = V/A, \tag{43}$$

where A is the total cross-sectional area of the bubble plume above a void fraction threshold, V is the volume of air entrained per unit width, and $\bar{\alpha}_b$ is the void fraction averaged over A. LM91 fitted functional expressions to computed values of A, V and $\bar{\alpha}$ which are used here for comparison to the model results. The data for V was fitted by

$$V/V_0 = 2.6\exp(-3.9(t-t_b)/T), \tag{44}$$

where V_0 is a reference value of the volume of air per unit width. In LM91 and Lamarre and Melville (1994), V_0 was evaluated as $V_0 = V(t = t_b + 0.2T)$ or by the maximum V.

The data for A was fitted by

$$A/V_0 = 325\left((t-t_b)/T\right)^{2.3}, \tag{45}$$

and $\bar{\alpha}_b$ was fitted by

$$\bar{\alpha}_b(\%) = 0.8\left((t-t_b)/T\right)^{-2.3}. \tag{46}$$

Note that, in the formula of LM91, $()^{-2/3}$ was given in (46) and is believed to be a typo.

We calculated A, V and $\bar{\alpha}_b$ from numerical results in the same way as in LM91. A and V were normalized by V_0 which is the maximum V in the numerical results. Figure 7 shows the normalized A, V and $\bar{\alpha}_b$ computed from the model results with comparisons to the data fitted curves. The threshold used in the calculations is 0.3%. Figure 7 (a) shows that the model predicted a parabolic-like evolution of the void fraction area A, which has a similar trend as shown by the data fitted curve. The area A was over-predicted at the beginning of wave breaking, and a more moderate increase in A can be found in the early time in the wave period, compared with the data fitted line. The comparison of the normalized air volume V/V_0 shown in Figure 7 (b) indicates an underprediction of air entrainment at the beginning of breaking, which is consistent with the absence of a large entrained pocket of air in the numerical simulation. In the first half wave period, the volume V/V_0 decreases more slowly than indicated by the data, resulting in overprediction of V/V_0 around the middle of the wave period. At later times, the decay rate of the air volume V/V_0 agrees reasonably well with data. Figure 7 (c) shows the void fraction averaged over the area A in comparison to the data-fitted curve (46). Again, an underprediction of the average void fraction can be found at the beginning of wave breaking, followed by overpredictions at later times. In general, the model predictions of the magnitude and evolutionary trend of the average void fraction are in reasonable agreement with the data. The underprediction at the beginning of wave breaking was expected because the model does not account for large air pockets in the continuum phase.

The horizontal and vertical centroids of the void-fraction distribution in the bubbly plume were also calculated using

$$(x_m, z_m) = \frac{\int_A \alpha_b(x, z) dA}{\int_A \alpha_b dA} \tag{47}$$

where x is the horizontal distance from x_b and z is the depth from the free surface. The top panel of Figure 8 shows the horizontal centroid normalized by the wave length λ_c corresponding to the central frequency f_c. The horizontal centroid moves at roughly the phase speed (slope of the dashed line) in the early stage after wave breaking and gradually slows down in the later time. Compared with the measurements in LM91 (Figure 3e in LM91), the model predicted the tendency of the x_m evolution but over-predicted the speed of the horizontal centroid in the later time. The normalized vertical centroid z_m is shown in the bottom panel of Figure 8. The vertical centroid is roughly constant, which is consistent with the measurements (Figure 3f in LM91). It was explained by Lamarre and Melville (1991) that the downward advection of fluid may balance the upward motion of the bubbles themselves.

According to observations in laboratory experiments, bubbles with different sizes make different contributions to the void fraction, with larger bubbles contributing more directly to higher void fraction values. The contributions of different size bubbles to void fraction can be demonstrated by the void fraction distribution calculated from each bubble group. Figure 9 shows snapshots of the void fractions contributed by group bins $r_b = 0.10, 0.55, 1.43$ and 6.16 mm at $(t - t_b)/T = 0.62$. Note that the radius bins are not evenly split based on bubble radius and thus the void fraction calculated from each bin may not represent the exact contribution from bubbles at specific size. However, the figure shows orders of magnitude differences in the void fractions contributed from different bins and indicates that bubbles larger than $O(1)$ mm make a major contribution to void fraction. Smaller bubbles do not contribute much to the total volume of air but contribute significantly to the cross-sectional area of the bubble cloud.

Two major discrepancies between the model and the data were observed in the predicted void fraction distribution with comparison to the bubble plume shape captured in the laboratory experiments (LM91; Lamarre and Melville, 1994). First, the core region of the high void fraction measured in the bubble plume is basically located in front of the wave surface peak where large air pockets take place. The model predicted the core region at the wave surface peak where the shear production is maximum. Second, the bubble plume represented by the predicted void fraction does not look like a semicylindrical plume as described in Lamarre and Melville (1994). The maximum void fraction does not appear at the air-water interface as shown in the measurements. The dislocation of the predicted core region of the high void fraction is probably due to the air entrainment algorithm formulated by the shear production which reaches maximum around the wave crest as shown in Figure 5. The model does not predict correctly large air pockets on the surface of the breaking bore, resulting in the under-prediction of void fraction at the air-water interface.

It is interesting to look at the moments calculated from different void fraction thresholds, as the moments calculated using a larger void fraction threshold reflect the evolution of larger bubble populations. Figure 10 shows the moments calculated from the void fraction thresholds 3% and 10% in addition to that from 0.3%. Apparently, the area bounded by a larger threshold is generally smaller than the area bounded by a smaller one as demonstrated in Figure 10 (a). A parabolic-like evolution can be also found in in the larger threshold cases. The area bounded by the threshold 10% starts to decrease earlier compared with the areas with 3% and 0.3% threshold, indicating the stronger degassing effects for larger bubbles. The decay rates of air volume calculated using different thresholds are shown in Figure 10 (b). As expected, the air volume from a larger threshold decays faster, especially for the case with a 10% threshold. The averaged void fractions $\bar{\alpha}_b$ with different void fraction threshold are shown in Figure 10 (c). For the 10% threshold, the averaged void fraction decays faster at the beginning of breaking, indicating that more larger size bubbles are contained in the sectional area bounded by the large threshold at the beginning and escape the water column due to degassing.

The evolution of bubble cloud can be measured by the retention time of bubbles in the water column. Figure 11 shows the evolution of bubble number integrated over the water column between $(x - x_b)/\lambda_c = 0$ and 1.0 for bubble group bins $r_b = 0.10, 0.34, 0.89, 2.33$, and 6.16 mm. The bubble numbers are normalized by the maximum bubble number during the time period of $(t - t_b)/T = 0 \sim 1.0$ for each bin. The figure shows that bubble counts for different bubble sizes reach maxima at different times and decay at different rates. For larger bubbles, such as $r_b = 2.33$ and 6.16 mm, bubble numbers reach their maxima when the turbulent production becomes most intense at $(t - t_b)/T = 0.2$, and then bubble numbers decay rapidly because the degassing process dominates over the bubble entrainment. For smaller bubbles, such as $r_b = 0.1$ and 0.34 mm, weak degassing causes accumulation of bubbles and results in the maxima at later times. The figure also indicates that a significant amount of smaller bubbles are retained in the water column at the end of a wave period.

Field and laboratory experiments (e.g., Deane and Stokes, 2002) revealed that the bubble size spectrum changes in both time and space during the evolution of bubble population. Figure 12 demonstrates the bubble size spectrum at four depths, $dk_c = 0.0749, 0.1233, 0.1720$, and 0.2207, where d is the depth below the surface of the wave crest at $(t - t_b)/T = 0.62$ and $(x - x_b)/\lambda_c = 0.5530$. In general, all slopes basically follow the input spectrum (Deane and Stokes, 2002) with slight increases with depth. The figure also indicates that bubbles with smaller sizes tend to penetrate deeper and stay longer in the water column, resulting in significant contribution to the cross-sectional area of the bubble cloud as measured in the laboratory experiments. After initial bubble entrainment, the bubble size spectrum depends on bubble evolution processes in the quiescent phase such as bubble further breakup, coalescence, degassing, dissolution, advection and diffusion under turbulent flow. The effects of those physical processes are modeled by the individual algorithms described in Section 2. Because of the lack of detailed measurements, those individual processes are not addressed in the paper.

4. CONCLUSION

The present work has been motivated by the need of an efficient physics-based numerical model for prediction of air bubble population in a surfzone-scale domain. Directly modeling of air bubble entrainment and evolution at this scale is computationally unaffordable. In this study, we proposed a two-fluid model in which the air entrainment is formulated by connecting the shear production at air-water interface and the bubble number intensity with a certain bubble size spectra as observed by Deane and Stokes (2002). The model fed with the initially entrained bubbles basically simulates bubble plumes, and requires much less spatial and temporal resolution than needed to capture detailed air entrainment process.

The two-fluid model was developed based on Buscaglia et al. (2002). A 2-D VOF RANS model with the $k-\epsilon$ turbulence closure was used to model the gas-liquid mixture phase. The bubble phase was modeled using the equation of bubble number density equation for a polydisperse bubble population. The two-fluid model takes into account bubble-induced turbulence effects and intergroup transfer through bubble coalescence and breakup processes.

The model was used to simulate breaking wave-induced bubble plumes measured by LM91. The air entrainment parameter calibrated using the maximum void fraction measured in the laboratory experiments resulted in reasonable agreements between the predicted and the measured moments of the void fraction field defined by LM91. The model predicted a parabolic-like evolution of the bubble area bounded by the 0.3% threshold of void fraction. The decay rates of air volume and averaged void fraction are generally consistent with the laboratory experiments. The model results revealed that bubbles larger than 1 mm make a major contribution to void fraction, while smaller bubbles contribute significantly to the cross-sectional area of the bubble cloud but do not contribute much to the total volume of air. A stronger degassing effect on larger bubbles is evidenced by the earlier drop of the bubble plume area and the faster decay of the air volume bounded by a larger void fraction threshold compared with those bounded by a smaller threshold.

The model with the calibrated parameter a_b underpredicted the void fraction at the beginning of breaking. The core region of the high void fraction was predicted at the wave surface peak where the shear production reaches maximum while the measurements show the core region in front of the wave surface peak where large air pockets occur. The maximum void fraction was not predicted at the air-water interface as in the measurements.

A primary source of discrepancies between observations and model behavior is the single-phase model used for the mixture phase and the algorithm used in the air entrainment formulation. The VOF model employed here does not account for the entrainment of identifiable gas pockets during the early stages of breaking, and the contribution of these pockets to initial average void fraction is absent. Our present research utilizes a model which incorporates a discrete air phase which can contribute to directly represented air pockets entrained by surface overturning or other folding effects. In addition, algorithms are being developed which will be utilized to move entrained air volumes from a discrete two-phase representation into the continuum multiphase representation, in order to continue computations without requiring the VOF algorithm to maintain the identity of larger entrained bubbles.

Acknowledgments

This study was supported by Office of Naval Research, Coastal Geosciences Program, grants N00014-07-1-0582, N00014-09-1-0853, and N00014-10-1-0088.

References

Baldy, S., 1993, “A generation-dispersion model of ambient and transient bubbles in the close vicinity of breaking waves”, *J. Geophys. Res.*, 98, 18277-18293.

Banerjee, S., 1990, Modeling considerations for turbulent multiphase flows. In: W. Rodi and E.N. Ganic, Editors, *Engineering Turbulence Modeling and Experiments*, Elsevier, New York (1990), pp. 831-866.

Buscaglia, G. C., Bombardelli, F. A., and Garcia, M H., 2002, Numerical modeling of large-scale bubble plumes accounting for mass transfer effects, *International Journal of Multiphase Flow*, 28, 1763-1785

Carrica, P. M., Bonetto, F., Drew, D. A., Lahey, R. T. Jr, 1998, The interaction of background ocean air bubbles with a surface ship, *Int. J. Numer. Meth. Fluids*, 28, 571-600.

Chen, P., Sanyal, J., and Duduković, M. P., 2005, Numerical simulation of bubble columns flows: effect of different breakup and coalescence closures, *Chemical Engineering Science*, 60, 1085-1101.

Clift, R., Grace, J., Weber, M., 1978, *Bubbles, Drops and Particles*, Academic Press.

Cox, D. and Shin, S., 2003, Laboratory measurements of void fraction and turbulence in the bore region of surf zone waves, *J. Eng. Mech.*, 129, 1197-1205

Deane, G. B. and Stokes, M. D., 2002, Scale dependence of bubble creation mechanisms in breaking waves, *Nature* 418, 839-844.

Drew, D and Passman, S., 1998, *Theory of multicomponent fluids*, Springer.

Garrett, C., Li M., and Farmer, D., 2000, The connection between bubble size spectra and energy dissipation rates in the upper ocean, *Journal of Physical Oceanography*, 30, 2163-2171.

Guido-Lavalle, G., Carrica, P., Clausse, A., and Qazi, M. K., 1944, A bubble number density constitutive equation, *Nuclear Engineering and Design*, 152, 1-3, 213-224.

Hinze, J. O., 1955, Fundamentals of the hydrodynamic mechanism of splitting in dispersion processes, *Amer. Inst. Chem. Eng. J.*, 1, 289-295.

Hoque, A, 2002. Air bubble entrainment by breaking waves and associated energy dissipation, PhD Thesis, Tokohashi University of Technology.

Kataoka, I. and Serizawa, A., 1989, Basic equations of turbulence in gas-liquid two-phase flow, *Int. J. Multiphase Flow* 15, pp. 843-855.

Kothe, D. B., Mjolsness, R. C. and Torrey, M. D., 1991, RIPPLE: a computer program for incompressible flows with free surfaces, Los Alamos National Laboratory, Report LA - 12007 - MS.

Lamarre, E. and Melville, W. K., 1994, Void-fraction measurements and sound-speed fields in bubble plumes generated by breaking waves, *J.*

Acoust. Soc. Am., 95 (3), 1317-1328.

Lamarre, E. and Melville, W. K., 1991, Air entrainment and dissipation in breaking waves, *Nature*, 351, 469-472.

Lasheras, J. C., Eastwood, C., Martínez-Bazán, and Montanñés, J. L., 2002, A review of statistical models for the break-up of an immiscible fluid immersed into a fully developed turbulent flow, *International Journal of Multiphase Flow*, 28, 247-278.

Leighton, T. G., Schneider, M. F., and White, P. R., 1994, Study of dimensions of bubble fragmentation using optical and acoustic techniques, *Proceedings of the Sea Surface Sound*, Lake Arrowhead, California, edited by M. J. Buckingham and J. Potter, World Scientific, Singapore, pp. 414428.

Lin, P. and Liu, P. L.-F, 1998, A numerical study of breaking waves in the surf zone, *J. Fluid Mech.*, 359, pp. 239-264.

Lin, P. and Liu, P. L.-F., 1999, Internal wave-maker for NavierStokes equation models, *J. Waterw. Port Coast. Ocean Eng.* 125 4, pp. 207-215.

Lopez de Bertodano, M., Lahey, R. T., and Jones, O. C., 1994, Development of a $k - \epsilon$ model for bubbly two-phase flow, *Journal of Fluids Engineering*, 116 (1), 128-134.

Luo, H. and Svendsen, H. F., 1996, "Theoretical model for drop and bubble breakup in turbulent dispersions", *AIChE J.*, 42, 1225-1233.

Luo, H., 1993, Coalescence, breakup and liquid circulation in bubble column reactors. D. Sc. Thesis, Norwegian Institute of Technology.

Ma, G., Shi, F., and Kirby, J. T., 2010, A polydisperse two-fluid model for surfzone bubble simulation, to be submitted to *J. Geophys. Res.*.

Martínez-Bazán, C., Montañes, J.L., Lasheras, J.C., 1999, On the break-up of an air bubble injected into a fully developed turbulent flow. Part I: Break-up frequency, *J. Fluid Mech.* 401, 157-182.

Moraga, F. F., Carrica, P. M., Drew, D. A., and Lahey Jr., R. T., 2008, A sub-grid air entrainment model for breaking bow waves and naval surface ships, *Computers and Fluids*, 37, 281-298.

Mori, N., Suzuki, T. and Kakuno, S., 2007, Experimental study of air bubbles and turbulence characteristics in the surf zone, *J. Geophy. Res.*, 112, C05014, doi:10.1029/2006JC003647.

Nadaoka, K., Hino, M. and Koyano, Y., 1989, Structure of turbulent flow field under breaking waves in the surf zone, *J. Fluid Mech.*, 204, 359-387.

Prince, M.J. and Blanch, H.W., 1990, Bubble coalescence and break-up in air-sparged bubble columns, *AICHE J.*, 36, 1485-1499

Rapp, R. J. and Melville, W. K., 1990, Laboratory measurements of deep-water breaking waves, *Philos. Trans. R. Soc. Lond. A*, 331, pp. 731-800.

Rodi, W, 1980, Turbulence Models and Their Application in Hydraulics - A State of the Art Review, IAHR, Delft, The Netherlands.

Sheng, Y. Y. and Irons, G. A., 1993, Measurement and modeling of turbulence in the gas/liquid two-phase zone during gas injection, *Metallurgical and Materials Transactions B*, 24B, pp. 695-705.

Shi, F., Zhao Q., Kirby J. T., Lee, D. S., and Seo S. N. 2004, Modeling wave interaction with complex coastal structures using an enhanced VOF model, *Proc. 29th Int. Conf. Coastal Engrng.*, Cardiff, 581-593.

Shi, F., Kirby, J. T., Haller, M. C. and Catalan, P., 2008, Modeling of surfzone bubbles using a multiphase VOF model, *Proc. 31st Int. Conf. Coastal Engrng.*, Hamburg, 157-169.

Smith, B. L., 1998, On the modelling of bubble plumes in a liquid pool, *Applied Mathematical Modelling*, 22, pp. 773-797.

Sokolichin, A, Eigenberger, G, and Lapin, A. 2004. Simulation of buoyancy driven bubbly flow: established simplifications and open questions. *AIChE J.*, 50, 24-45.

Terrill, E. J., Melville, W. K., and Stramski, D., 2001, Bubble entrainment by breaking waves and their influence on optical scattering in the upper ocean, *J. Geophys. Res.*, 106, C8, 16,815-16,823.

Thorpe, S. A., 1982, On the clouds of bubbles formed by breaking wind-waves in deep water, and their role in air-sea gas transfer, *Phil. Trans.*

Roy. Soc. London A, 304, 155-210.

van den Hengel, E.I.V., Deen, N.G., Kuipers, J.A.M., 2005, Application of coalescence and breakup models in a discrete bubble model for bubble columns. *Ind. Eng. Chem. Res.*, 44, 5233-5245.

Zhao, Q., Armfield, S., and Tanimoto, K., 2004, Numerical simulation of breaking waves by a mult-scale turbulence model, *Coastal Engineering*, 51, 53-80.

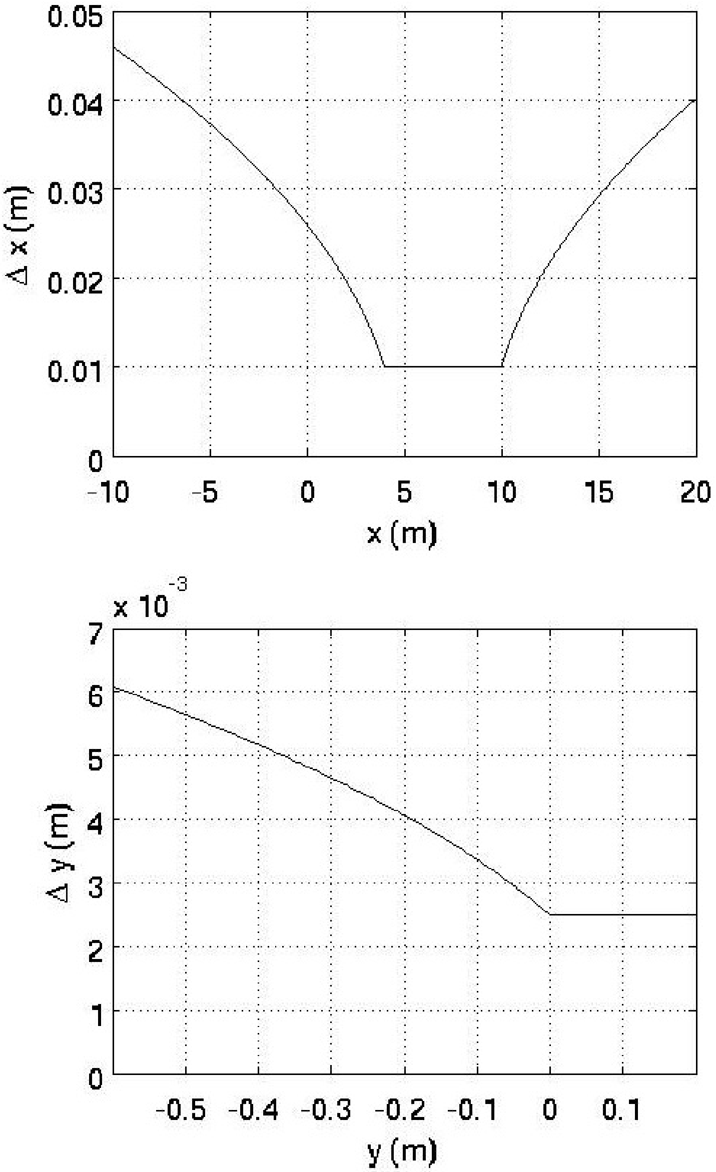

Figure 1: Grid spacing in x direction (top) and y direction (bottom).

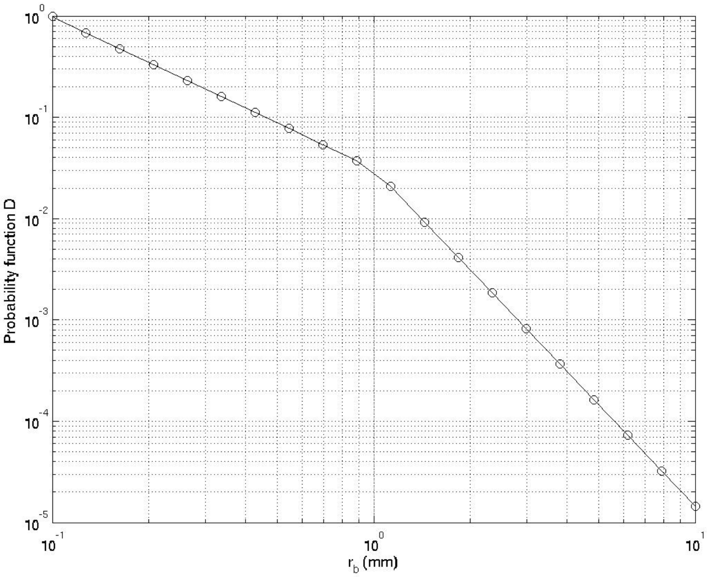

Figure 2: Bubble size probability density function D (circles represent values at 10 radius bins in the present application).

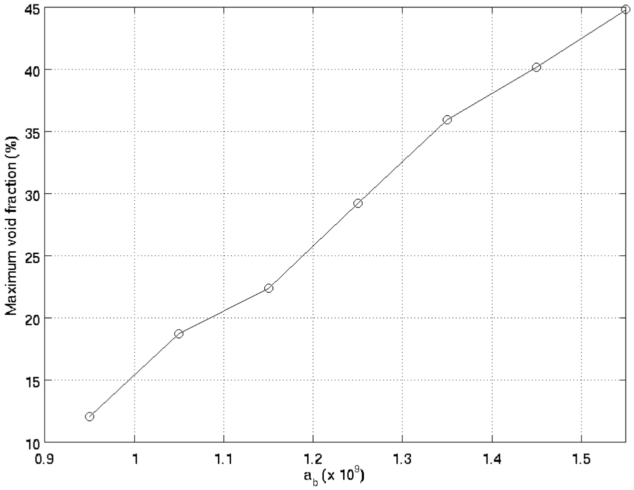

Figure 3: Maximum void fractions from test runs with different a_b.

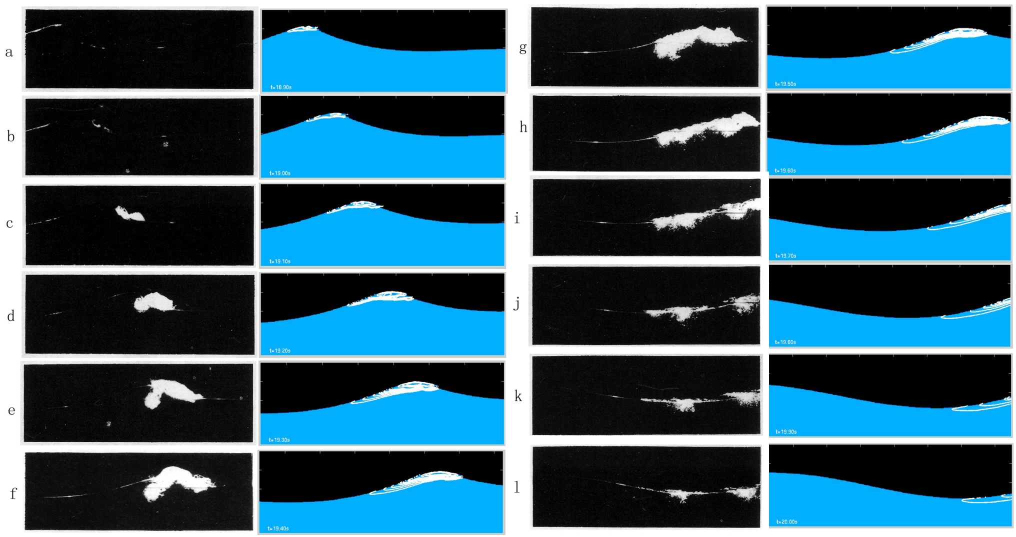

Figure 4: Photographs of the breaking wave and bubble cloud (first and third column) in Rapp and Melville (1990) versus predicted wave surface and void fraction contours above 0.1% in the case of $f_c = 0.88$ Hz, $ak_c = 0.352$, and $\Delta f/f_c = 0.73$. Time is from 18.90 to 20.40 s with 0.10 s interval.

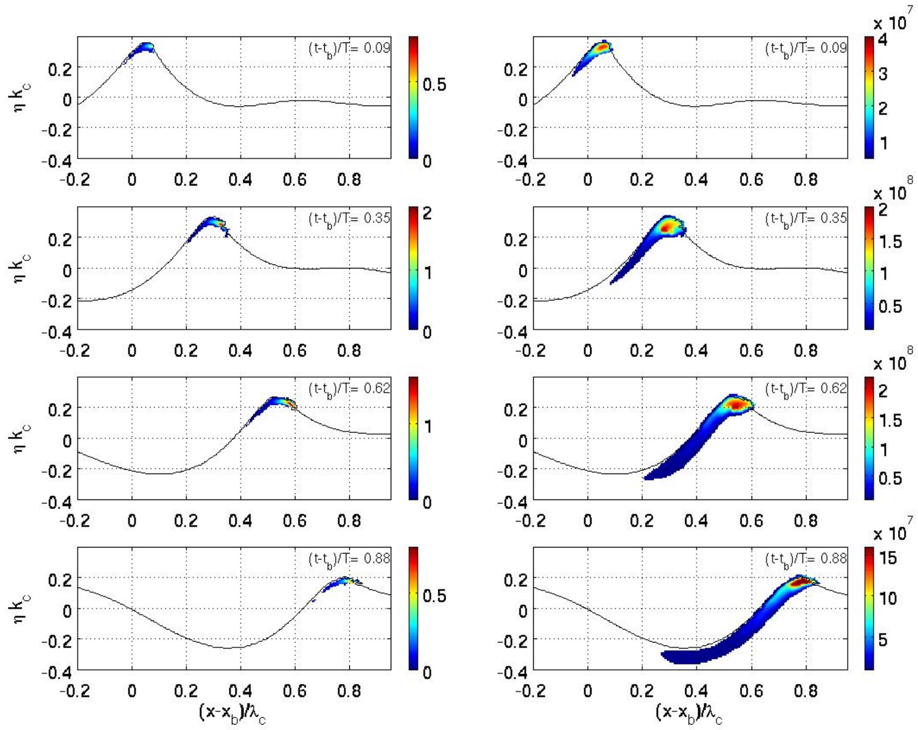

Figure 5: Left: shear production above the threshold $P_{r0} = 0.02 m^2/s^3$, right: bubble number density above 5×10^6 per m^3, at $(t - t_b)/T = 0.09, 0.35, 0.62$ and 0.88. Case: $f_c = 0.88$ Hz, $ak_c = 0.38$, and $\Delta f / f_c = 0.73$.

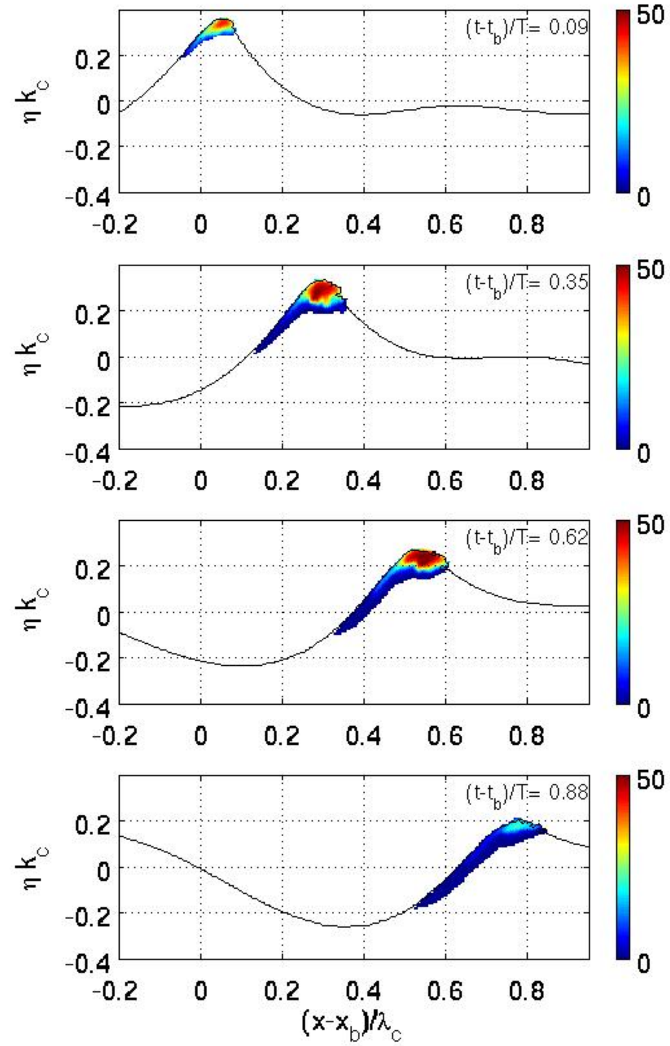

Figure 6: Void fraction larger than the threshold 0.3% at $(t - t_b)/T = 0.09, 0.35, 0.62$ and 0.88 in the case of $f_c = 0.88$ Hz, $ak_c = 0.38$, and $\Delta f/f_c = 0.73$.

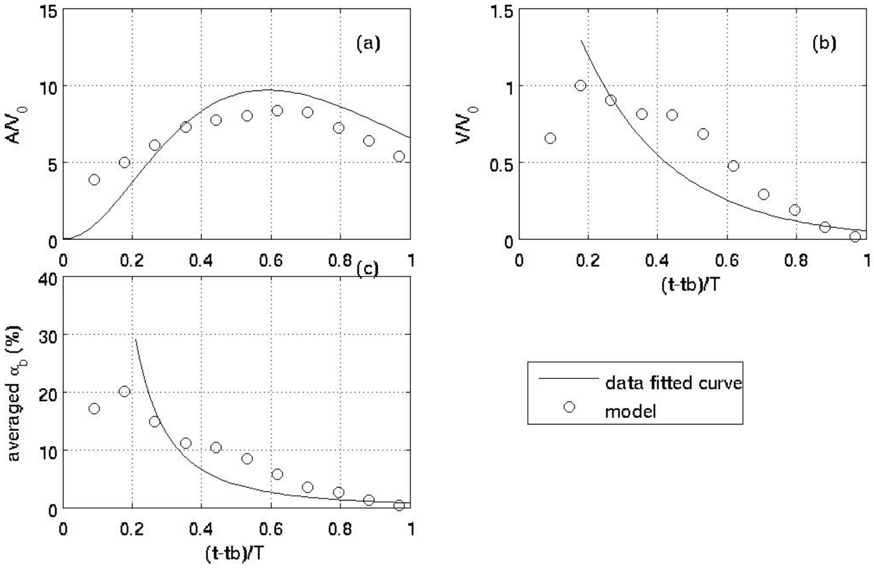

Figure 7: Moments calculated using the void fraction threshold of 0.3%, (a) Cross-sectional area A of bubble plume normalized by V_0; (b) Air volume V normalized by V_0; (c) Mean void fraction $\bar{\alpha}_b$. Case: $f_c = 0.88$ Hz, $ak_c = 0.38$, and $\Delta f/f_c = 0.73$. Solid curves are functional fits to laboratory data from LM91. Model results shown as open circles.

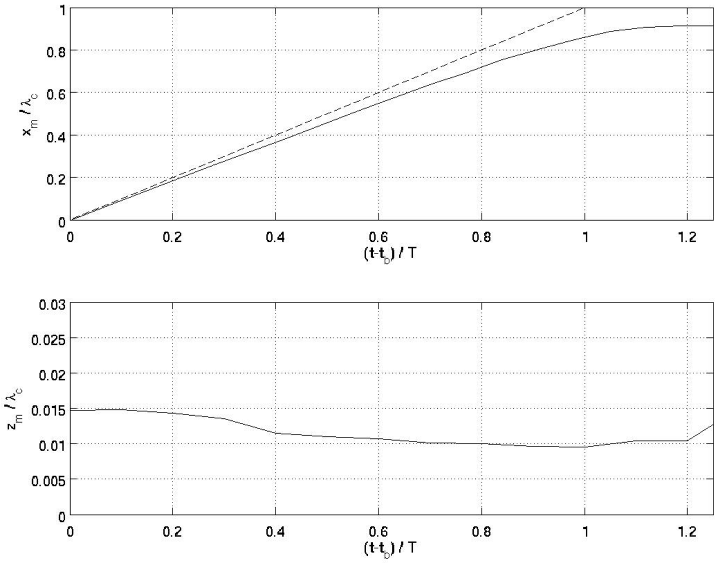

Figure 8: The horizontal centroid (top) and vertical centroid (bottom) normalized by wave length.

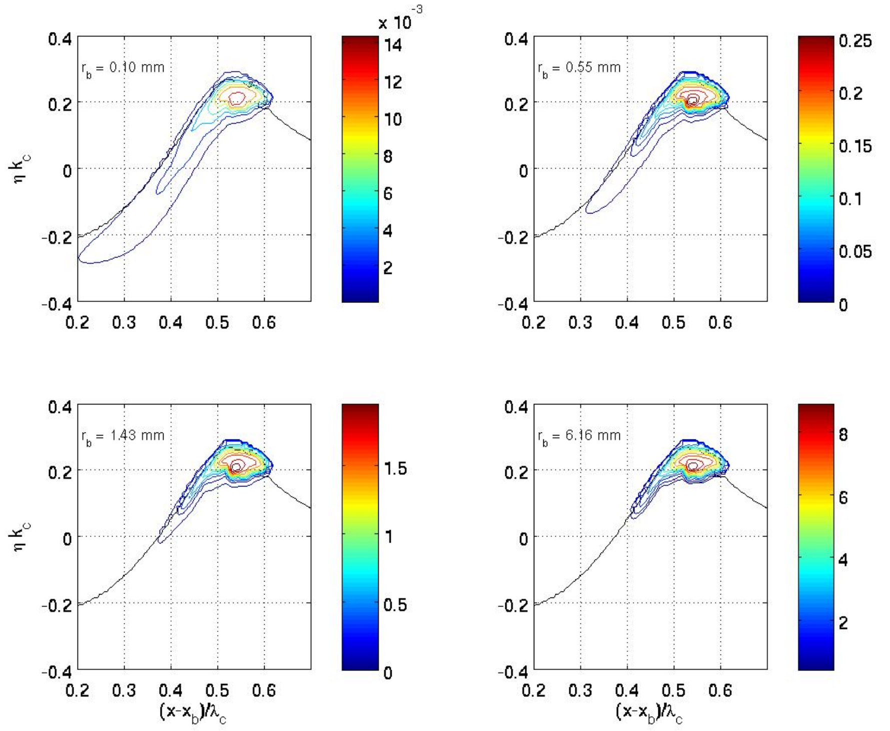

Figure 9: Void fraction (color contours %) contributed from group bins $r_b = 0.10, 0.55, 1.43$ and 6.16 mm in the case of $f_c = 0.88$ Hz, $ak_c = 0.38$, and $\Delta f/f_c = 0.73$.

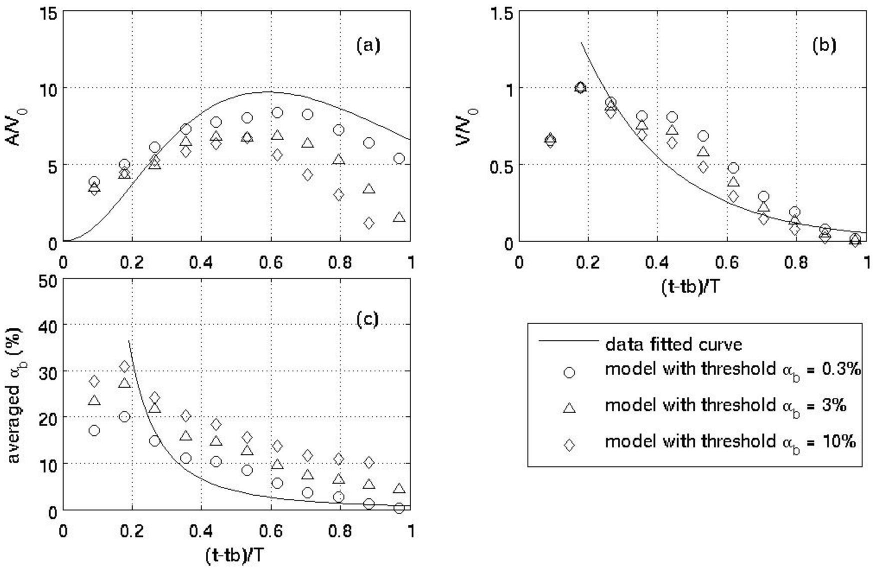

Figure 10: Moments calculated using the void fraction threshold of $0.3\%, 3\%$ and 10%, (a) Cross-sectional area A of bubble plume normalized by V_0; (b) Air volume V normalized by V_0; (c) Mean void fraction $\bar{\alpha}_b$. Case: $f_c = 0.88$ Hz, $ak_c = 0.38$, and $\Delta f/f_c = 0.73$.

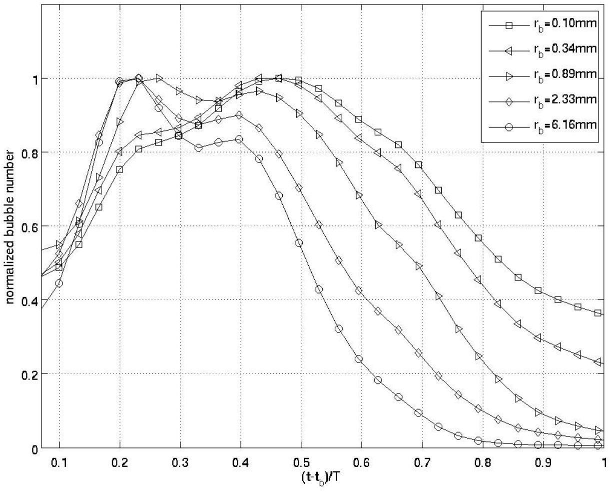

Figure 11: Evolutions of normalized bubble numbers in the water column between $(x - x_b)/\lambda_c = 0$ and 2.5 for bubble group bins $r_b = 0.10, 0.34, 0.89, 2.33$ and 6.16 mm.

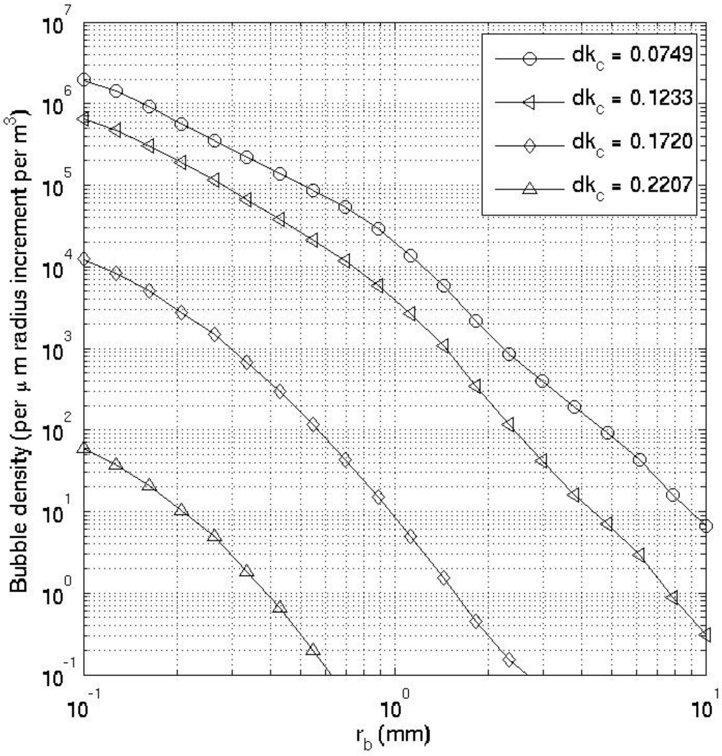

Figure 12: Bubble size spectrum at depth $dk_c = 0.0749, 0.1233, 0.1720$, and 0.2207 from the wave surface, at $(x - x_b)/\lambda_c = 0.5530$ and $(t - t_b)/T = 0.62$